A C^0-discontinuous Galerkin method for the stationary quasi-geostrophic equations of the ocean

Tae-Yeon Kim[a,*], Eun-Jae Park[b], Dong-wook Shin[b]

[a] *Civil Infrastructure and Environmental Engineering, Khalifa University of Science, Technology and Research, Abu Dhabi, 127788, United Arab Emirates*
[b] *Department of Computational Science and Engineering, Yonsei University, Seoul 03722, Republic of Korea*

Abstract

This work concerns the development of a finite-element algorithm for the stationary quasi-geostrophic equations to treat the large scale wind-driven ocean circulation. The algorithm is developed based on the streamfunction formulation involving fourth-order gradients of the streamfunction. Here, we examine the adaptation of a relatively inexpensive, nonconforming method based on C^0 basis functions. We develop the variational form of the method and establish consistency. The method weakly enforces continuity of the normal flux across interelement boundaries and stabilization is achieved via Nitsche's method. Explicit expression for the choice of the stabilization parameter is derived. Moreover, the theoretical error estimate for the linear Stommel–Munk model is performed. Numerical results from several benchmark problems on rectangular and curved domains are provided to demonstrate the accuracy and robustness of the method. We also provide the Mediterranean sea example to demonstrate the capability of the approach to the wind-driven ocean circulation simulation.
© 2015 Elsevier B.V. All rights reserved.

1. Introduction

The large scale wind-driven ocean currents play an important role in understanding the climate system because they transport heat around the globe (Dijkstra [1] and Ghil et al. [2]). These currents are characterized by the wind forcing and the effects of rotation. Annual wind patterns are westward near the equator and eastward at the midlatitudes. These wind patterns derive strong western boundary currents such as the Gulf stream and the Labrador current in the north Atlantic and the Kuroshio and Oyashio currents in the north Pacific. Typical phenomena of these currents are strong western boundary currents, weak interior flows, and weak eastern boundary currents.

One of the popular mathematical models for the study of the wind-driven ocean circulation is the quasi-geostrophic equations (QGE) (Vallis [3], Cushman-Roisin and Beckers [4], Majda [5], Majda and Wang [6], Pedlosky [7],

* Corresponding author.
E-mail addresses: taeyeon.kim@kustar.ac.ae (T.-Y. Kim), ejpark@yonsei.ac.kr (E.-J. Park), d_shin@yonsei.ac.kr (D.-w. Shin).

McWilliams [8]). The QGE allow for efficient computational simulations while preserving many of the typical features of the underlying large scale ocean flows. The purpose of this study is to develop a relatively inexpensive nonconforming finite-element method of the QGE for the simulation of the wind-driven oceanic flows on irregular geometries.

Rather than the streamfunction formulation, most finite-element methods of the QGE have been performed based on the streamfunction–vorticity formulation. This is because the streamfunction–vorticity formulation is a second-order partial-differential equation (PDE). Thus, its conforming finite-element discretization requires easy-to-implement low-order C^0-elements. The streamfunction–vorticity formulation has two unknown variables, the potential vorticity and the streamfunction. Moreover, to the best of our knowledge, its available error estimates are suboptimal (Fix [9]). On the other hand, the streamfunction formulation of the QGE is a fourth-order PDE for one unknown, the streamfunction. Hence, a standard conforming finite-element approximation requires higher-order C^1-elements such that both the streamfunction and its first derivatives are continuous across element interfaces. Our study focuses on the streamfunction formulation with optimal error estimates.

Several finite-element methods for the streamfunction formulation have been developed. Recently, conforming finite-element discretizations with C^1-elements using the Argyris triangular element (Foster et al. [10]) and B-splines (Kim et al. [11]) have been introduced. Furthermore, Jiang and Kim [12] modeled arbitrary shaped coastal boundaries on embedded boundaries based on the B-spline finite-element algorithm. The Argyris triangular element is not efficient because it involves 21 degrees of freedom including six degrees of freedom (the value of the streamfunction and the values of its first, second, and mixed derivatives) at each vertex and one degree of freedom (the value of normal derivative of the streamfunction) at each of the edge midpoints. Whereas B-splines can be easily constructed over rectilinear domains, their use with arbitrarily shaped domains often involves either a mapping (as with isogeometrics) or a 'fictitious-domain' type of approaches (Höllig [13]). More importantly, B-splines are non-interpolatory and, thus, imposing even simple Dirichlet boundary conditions can be problematic.

The main goal of the paper is to present variational formulations using C^0-elements to discretize the streamfunction formulation of the stationary quasi-geostrophic equations (SQGE) and the Stommel–Munk model. The weak enforcement of continuity of the derivatives across element interfaces is achieved via Nitsche's [14] method. The idea of Nitsche' method is to simply replace the Lagrange multipliers with their physical representation, namely the normal flux at the element interface. Moreover, an additional penalty like term is incorporated to restore the coercivity of the variational form. Our approach is relevant to a consistent C^0-interior penalty method which was presented by Engel et al. [15] for beam and plate theories and strain gradient theory and further developed by Brenner et al. [16,17], Wells and Dung [18], and Hansbo et al. [19].

Baker [20] first employed Nitsche's method to develop a nonconforming finite-element formulation for a fourth-order elliptic problem. Recently, Nitsche's method has been successfully applied for weakly imposing Dirichlet boundary conditions in standard finite-element methods for second- and fourth-order PDEs (Embar et al. [21], Embar et al. [22], and Kim et al. [23]), a meshfree method (Fernandez-Mendez and Huerta [24]), and embedded finite-element methods (Hansbo and Hansbo [25] and Dolbow and Harari [26]). Moreover, this method has also been used with success for finite-element discretizations of a second-gradient theory based on low-order C^0-elements (Kim et al. [27], Kim and Dolbow [28], and Kim et al. [29]).

The remainder of the paper is organized as follows. In Section 2, we briefly present the SQGE. In Section 3, we develop variational formulations based on Nitsche's method for the SQGE as well as the linear Stommel–Munk model, along with the demonstrations of their variational consistency. Stability of the method is proved and the explicit lower bound of the stabilization parameter is derived. We also provide the theoretical error estimate for the linear Stommel–Munk model. Our presentation makes use of the existing results of continuous/discontinuous Galerkin finite-element methods (Brenner and Scott [30] and Shin et al. [31]). In Section 4, numerical studies are performed for these Nitsche-type formulations. Finally, in Section 5, we provide conclusions and a summary of directions for future work.

2. Streamfunction formulation of the SQGE

We consider a plane domain Ω with boundary Γ. For the study of the wind-driven circulation in an enclosed and midlatitude basin, the streamfunction formulation of the one-layer SQGE (Foster et al. [10]) is given by

$$Re^{-1}\Delta^2\psi + J(\psi, \Delta\psi) - Ro^{-1}\frac{\partial\psi}{\partial x} = Ro^{-1}F \quad \text{on } \Omega, \tag{1}$$

where ψ is the velocity streamfunction, F is the forcing, and

$$J(\psi, \Delta\psi) := \frac{\partial\psi}{\partial x}\frac{\partial\Delta\psi}{\partial y} - \frac{\partial\psi}{\partial y}\frac{\partial\Delta\psi}{\partial x} \qquad (2)$$

is the Jacobian operator. As usual, the parameters Re and Ro appearing in (1) denote the Reynolds and Rossby numbers, defined here by

$$Re = \frac{UL}{A} \quad \text{and} \quad Ro = \frac{U}{\beta L^2}, \qquad (3)$$

respectively, where β is the coefficient multiplying the y-coordinate in the β-plane approximation (see, for example, Vallis [3, Section 2.3.2] or Cushman-Roisin and Beckers [4]), A is the eddy viscosity parametrization, U is the characteristic velocity, and L is the characteristic length scale. In the one-layer SQGE, the flow is assumed to be homogeneous in the vertical direction. Stratification effects are therefore neglected in this model.

As in the two-dimensional Navier–Stokes equations, the Reynolds number Re is the coefficient of the diffusion term $\Delta^2\psi$. Therefore, with increasing Re, the magnitude of the diffusion term becomes smaller in comparison to the magnitude of the nonlinear convective term $J(\psi, \Delta\psi)$. The Rossby number Ro, which is absent from the two-dimensional Navier–Stokes equations, quantifies the rotation effects in the QGE and SQGE. For small Ro, which corresponds to large rotation effects, the forcing term $Ro^{-1}F$ becomes large compared with the other terms. Moreover, as Ro decreases, the effect of the term $Ro^{-1}\partial\psi/\partial x$, which can be interpreted as a convective contribution to the governing equation, becomes significant. For large scale oceanic flows, Re is large and Ro is small (i.e., small diffusion and large rotation, respectively) and, thus, the SQGE are dominated by convective terms with large forcing.

To close the model, we supplement the fourth-order partial-differential equation (1) with the boundary conditions

$$\psi = 0 \quad \text{and} \quad \nabla\psi \cdot \mathbf{n} = 0 \quad \text{on } \partial\Omega, \qquad (4)$$

where $\mathbf{n}$ represents the unit normal vector on the boundary $\partial\Omega$ directed outward from Ω. These boundary conditions are commonly used for the numerical studies of the two-dimensional Navier–Stokes equations (Gunzburger [32], Fairag [33], Fairag and Almulla [34]) and the SQGE (Foster et al. [10]). More careful discussions of boundary conditions are provided by Vallis [3] and Cummins [35].

3. Variational formulations for C^0-elements

In this section, we derive variational formulations for the finite-element discretization of the SQGE and the Stommel–Munk model using C^0-elements. We first introduce the space of admissible solution and test fields as

$$\mathcal{S} := H_0^2(\Omega) = \left\{ \psi \in H^2(\Omega) : \psi = \nabla\psi \cdot \mathbf{n} = 0 \text{ on } \partial\Omega \right\}. \qquad (5)$$

Multiplying (1) by a test function $\chi \in \mathcal{S}$, integrating over domain Ω, and using the divergence theorem, we obtain the weak formulation of the SQGE in the streamfunction formulation: Find $\psi \in \mathcal{S}$ such that

$$Re^{-1}\int_\Omega \Delta\psi\,\Delta\chi\,\mathrm{d}\boldsymbol{x} + \int_\Omega \Delta\psi\,(\psi_y\chi_x - \psi_x\chi_y)\,\mathrm{d}\boldsymbol{x} - Ro^{-1}\int_\Omega \psi_x\chi\,\mathrm{d}\boldsymbol{x} = Ro^{-1}\int_\Omega F\chi\,\mathrm{d}\boldsymbol{x} \qquad (6)$$

for all $\chi \in \mathcal{S}$. Here, $(\cdot)_x$ and $(\cdot)_y$ in the nonlinear term denote the derivatives with respect to x and y, respectively.

3.1. Finite-element discretization of the SQGE

In this section, we introduce our numerical formulation for the SQGE based on Nitsche's method. In this approach, the basis functions are C^0-continuous — so that their first and higher-order derivatives are discontinuous. Continuity of the first and higher-order derivatives is weakly enforced by adding weighted residual terms to the variational equation on element boundaries and invoking stabilization techniques.

To construct the bases, we consider a regular finite-element partition $\Omega^h = \cup_{i=1}^M \Omega_i$, with $\Omega^h \approx \Omega$ and M the total number of elements in the mesh. We choose approximation functions which are continuous on the entire domain but

discontinuous in first and higher-order derivatives across element boundaries. These functions belong to the function space $\mathcal{S}^h$ defined as

$$\mathcal{S}^h = \{\psi^h \in H_0^1(\Omega) : \psi^h|_{\Omega_i} \in P_k(\Omega_i) \text{ for each } i = 1, \ldots, M\}$$

where $P_k(\Omega_i)$ is the space of standard Lagrange polynomials of degree $\leq k$ ($k \geq 2$) on Ω_i. We note that $\mathcal{S}^h$ is a nonconforming approximation of $\mathcal{S}$, i.e., $\mathcal{S}^h \not\subset \mathcal{S}$.

Let us denote the set of element interiors by $\widetilde{\Omega}$ and the set of all edges by $\widetilde{\Gamma}$. For simplicity, let us define the integration over $\widetilde{\Omega}$ as

$$\int_{\widetilde{\Omega}} \psi \, \mathrm{d}\boldsymbol{x} = \sum_{\Omega_i \in \widetilde{\Omega}} \int_{\Omega_i} \psi \, \mathrm{d}\boldsymbol{x}$$

and the integration over $\widetilde{\Gamma}$ as

$$\int_{\widetilde{\Gamma}} \psi \, \mathrm{d}s = \sum_{e \in \widetilde{\Gamma}} \int_e \psi \, \mathrm{d}s$$

where e is the element edge.

The variational formulation of the SQGE based on Nitsche's method can be stated as: Find $\psi^h \in \mathcal{S}^h$ such that

$$a(\psi^h, \chi^h) = \ell(\chi^h) \tag{7}$$

for a test function $\chi^h \in \mathcal{S}^h$, where $a(\cdot, \cdot)$ and $\ell(\cdot)$ are defined in accord with

$$
\begin{aligned}
a(\psi^h, \chi^h) = \ & Re^{-1} \int_{\widetilde{\Omega}} \Delta\psi^h \Delta\chi^h \, \mathrm{d}\boldsymbol{x} + \int_{\widetilde{\Omega}} \Delta\psi^h (\psi_y^h \chi_x^h - \psi_x^h \chi_y^h) \, \mathrm{d}\boldsymbol{x} \\
& - Re^{-1} \left(\int_{\widetilde{\Gamma}} \langle\!\langle \Delta\psi^h \rangle\!\rangle [\![\nabla\chi^h \cdot \mathbf{n}]\!] \, \mathrm{d}s + \int_{\widetilde{\Gamma}} [\![\nabla\psi^h \cdot \mathbf{n}]\!] \langle\!\langle \Delta\chi^h \rangle\!\rangle \, \mathrm{d}s \right) \\
& + Re^{-1} \int_{\widetilde{\Gamma}} \frac{\eta}{|e|} [\![\nabla\psi^h \cdot \mathbf{n}]\!] [\![\nabla\chi^h \cdot \mathbf{n}]\!] \, \mathrm{d}s - Ro^{-1} \int_{\widetilde{\Omega}} \frac{\partial\psi^h}{\partial x} \chi^h \, \mathrm{d}\boldsymbol{x}
\end{aligned}
\tag{8}
$$

and

$$\ell(\chi^h) = Ro^{-1} \int_{\widetilde{\Omega}} F \chi^h \, \mathrm{d}\boldsymbol{x} \tag{9}$$

where $|e|$ is the characteristic size of the element edge e. Here, $[\![a]\!]$ and $\langle\!\langle a \rangle\!\rangle$ represent respectively the jump and average operators for a scalar function a on an element edge. While the second term on the second line of (8) weakly imposes continuity of the normal flux across element boundaries, the first term on the second line is required to impart a variational consistency. The first term of the third line is the stabilization term involving the stabilization parameter $Re^{-1}\eta/|e|$ for the interelement boundaries, where η is the proportionality constant. We start with the following trace inequality to compute the explicit lower bound of the parameter η.

Lemma 3.1 (*Trace Inequality*). *For a planar triangular element Ω_i, let h_{Ω_i} be the diameter of Ω_i, $|\partial\Omega_i|$ be the perimeter length of Ω_i, and $|\Omega_i|$ be the area of Ω_i. Then for all $\varphi \in P_k(\Omega_i)$, the following result holds*

$$\|\varphi\|_{0,\partial\Omega_i} \leq c_{k,\Omega_i} h_{\Omega_i}^{-1/2} \|\varphi\|_{0,\Omega_i},$$

where

$$c_{k,\Omega_i} = \sqrt{\frac{(k+1)(k+2)}{2} \frac{|\partial\Omega_i|}{|\Omega_i|} h_{\Omega_i}}. \tag{10}$$

The proof of Lemma 3.1 can be found in [36]. This result implies

$$\|\Delta\psi^h\|_{0,\partial\Omega_i} \leq c_{k-2,\Omega_i} h_{\Omega_i}^{-1/2} \|\Delta\psi^h\|_{0,\Omega_i} \quad \forall \psi^h \in P_k(\Omega_i). \tag{11}$$

Then the parameter η can be determined explicitly as in the following theorem.

Theorem 3.2 (*Coercivity*). *Let us define* $\eta_0 = 2\max_{\Omega_i \in \widetilde{\Omega}} c^2_{k-2,\Omega_i}$ *with* c_{k-2,Ω_i} *defined as in* (10). *Then for all* $\psi^h \in \mathcal{S}^h$ *and* $\eta \geq \eta_0$, *we have*

$$a(\psi^h, \psi^h) \geq \frac{1}{2}Re^{-1}\left(\sum_{\Omega_i \in \widetilde{\Omega}} \|\Delta\psi^h\|^2_{0,\Omega_i} + \sum_{e \in \widetilde{\Gamma}} \frac{\eta}{|e|}\|[\![\nabla\psi^h \cdot \mathbf{n}]\!]\|^2_{0,e}\right). \tag{12}$$

Proof. Set $\chi^h = \psi^h$ in (8),

$$
\begin{aligned}
a(\psi^h, \psi^h) = {}& Re^{-1}\sum_{\Omega_i \in \widetilde{\Omega}} \int_{\Omega_i} \Delta\psi^h \Delta\psi^h \, d\mathbf{x} + \int_{\widetilde{\Omega}} \Delta\psi^h(\psi^h_y \psi^h_x - \psi^h_x \psi^h_y) \, d\mathbf{x} \\
& - Re^{-1}\sum_{e \in \widetilde{\Gamma}} \left(\int_e \langle\!\langle \Delta\psi^h \rangle\!\rangle [\![\nabla\psi^h \cdot \mathbf{n}]\!] \, ds + \int_e [\![\nabla\psi^h \cdot \mathbf{n}]\!] \langle\!\langle \Delta\psi^h \rangle\!\rangle \, ds\right) \\
& + Re^{-1}\sum_{e \in \widetilde{\Gamma}} \frac{\eta}{|e|}\int_e [\![\nabla\psi^h \cdot \mathbf{n}]\!][\![\nabla\psi^h \cdot \mathbf{n}]\!] \, ds - Ro^{-1}\int_{\widetilde{\Omega}} \frac{\partial\psi^h}{\partial x}\psi^h \, d\mathbf{x} \\
\geq {}& Re^{-1}\sum_{\Omega_i \in \widetilde{\Omega}} \|\Delta\psi^h\|^2_{0,\Omega_i} - \left|2Re^{-1}\sum_{e \in \widetilde{\Gamma}} \int_e \langle\!\langle \Delta\psi^h \rangle\!\rangle [\![\nabla\psi^h \cdot \mathbf{n}]\!] \, ds\right| \\
& + Re^{-1}\sum_{e \in \widetilde{\Gamma}} \frac{\eta}{|e|}\|[\![\nabla\psi^h \cdot \mathbf{n}]\!]\|^2_{0,e} - Ro^{-1}\int_{\widetilde{\Omega}} \frac{\partial\psi^h}{\partial x}\psi^h \, d\mathbf{x}.
\end{aligned}
\tag{13}
$$

Young's inequality and (11) yield that

$$
\begin{aligned}
\left|2\sum_{e \in \widetilde{\Gamma}} \int_e \langle\!\langle \Delta\psi^h \rangle\!\rangle [\![\nabla\psi^h \cdot \mathbf{n}]\!] \, ds\right| &\leq 2\sum_{e \in \widetilde{\Gamma}} \int_e \left(\frac{|e|}{2\alpha\eta}\langle\!\langle \Delta\psi^h \rangle\!\rangle^2 + \frac{\alpha\eta}{2|e|}[\![\nabla\psi^h \cdot \mathbf{n}]\!]^2\right) ds \\
&\leq \sum_{\Omega_i \in \widetilde{\Omega}} \frac{h_{\Omega_i}}{2\alpha\eta}\|\Delta\psi^h\|^2_{0,\partial\Omega_i} + \sum_{e \in \widetilde{\Gamma}} \alpha\frac{\eta}{|e|}\|[\![\nabla\psi^h \cdot \mathbf{n}]\!]\|^2_{0,e} \\
&\leq \sum_{\Omega_i \in \widetilde{\Omega}} \frac{c^2_{k-2,\Omega_i}}{2\alpha\eta}\|\Delta\psi^h\|^2_{0,\Omega_i} + \sum_{e \in \widetilde{\Gamma}} \alpha\frac{\eta}{|e|}\|[\![\nabla\psi^h \cdot \mathbf{n}]\!]\|^2_{0,e} \\
&\leq \frac{1}{4\alpha}\sum_{\Omega_i \in \widetilde{\Omega}} \|\Delta\psi^h\|^2_{0,\Omega_i} + \alpha\sum_{e \in \widetilde{\Gamma}} \frac{\eta}{|e|}\|[\![\nabla\psi^h \cdot \mathbf{n}]\!]\|^2_{0,e}
\end{aligned}
\tag{14}
$$

where α is a positive constant. The last upper bound can be obtained using $\eta \geq \eta_0$. Using the divergence theorem and the boundary condition, we have

$$
\begin{aligned}
\int_{\widetilde{\Omega}} \frac{\partial\psi^h}{\partial x}\psi^h \, d\mathbf{x} &= \int_{\widetilde{\Omega}} \frac{1}{2}\frac{\partial}{\partial x}(\psi^h)^2 \, d\mathbf{x} \\
&= \frac{1}{2}\int_{\widetilde{\Omega}} \nabla\cdot((\psi^h)^2, 0) \, d\mathbf{x} = \frac{1}{2}\int_{\partial\Omega} (\psi^h)^2 n_1 \, ds = 0,
\end{aligned}
\tag{15}
$$

where n_1 is the first component of the outward normal vector $\mathbf{n}$. Applying (14) and (15) into (13) results in

$$a(\psi^h, \psi^h) \geq Re^{-1}\left(1 - \frac{1}{4\alpha}\right)\sum_{\Omega_i \in \widetilde{\Omega}} \|\Delta\psi^h\|^2_{0,\Omega_i} + Re^{-1}(1-\alpha)\sum_{e \in \widetilde{\Gamma}} \frac{\eta}{|e|}\|[\![\nabla\psi^h \cdot \mathbf{n}]\!]\|^2_{0,e}. \tag{16}$$

To ensure the coercivity, α must satisfy $1/4 < \alpha < 1$. Then Theorem 3.2 holds by choosing $\alpha = 1/2$. $\quad\square$

3.1.1. Proof of consistency

In contrast to a standard penalty method, our formulation is variationally consistent in the sense that solutions to (7) can provide solutions to the SQGE (1). The proof of consistency is provided based on Engel et al. [15]. The consistency of the method is derived through successive application of the divergence theorem to (7).

Let $\psi \in H^4(\Omega) \cap H_0^2(\Omega)$, then $[\![\Delta\psi]\!] = [\![\nabla(\Delta\psi) \cdot \mathbf{n}]\!] = 0$ on $\forall e \in \widetilde{\Gamma}$. Using these properties, we have

$$
\begin{aligned}
\int_{\Omega} \Delta\psi \Delta\chi^h \, d\mathbf{x} &= -\int_{\widetilde{\Omega}} \nabla(\Delta\psi) \cdot \nabla\chi^h \, d\mathbf{x} + \int_{\widetilde{\Gamma}} [\![\Delta\psi \nabla\chi^h \cdot \mathbf{n}]\!] \, ds \\
&= \int_{\widetilde{\Omega}} \Delta^2\psi \chi^h \, d\mathbf{x} - \int_{\widetilde{\Gamma}} [\![\nabla(\Delta\psi) \cdot \mathbf{n}\chi^h]\!] \, ds + \int_{\widetilde{\Gamma}} \langle\!\langle\Delta\psi\rangle\!\rangle [\![\nabla\chi^h \cdot \mathbf{n}]\!] \, ds \\
&= \int_{\widetilde{\Omega}} \Delta^2\psi \chi^h \, d\mathbf{x} + \int_{\widetilde{\Gamma}} \langle\!\langle\Delta\psi\rangle\!\rangle [\![\nabla\chi^h \cdot \mathbf{n}]\!] \, ds
\end{aligned}
\tag{17}
$$

where we have taken advantage of the equality

$$
[\![ab]\!] = [\![a]\!]\langle\!\langle b\rangle\!\rangle + \langle\!\langle a\rangle\!\rangle[\![b]\!],
\tag{18}
$$

which holds for all a and b. By repeatedly applying integration by parts to the second term of (8), we obtain the identity

$$
\int_{\widetilde{\Omega}} \Delta\psi (\psi_y \chi_x^h - \psi_x \chi_y^h) \, d\mathbf{x} = \int_{\widetilde{\Omega}} (\psi_x (\Delta\psi)_y - \psi_y (\Delta\psi)_x) \chi^h \, d\mathbf{x}.
\tag{19}
$$

Applying (17), (19), and the property $[\![\nabla\psi \cdot \mathbf{n}]\!] = 0$ to (8) yields

$$
a(\psi, \chi^h) = \int_{\widetilde{\Omega}} \left(Re^{-1}\Delta^2\psi + J(\psi, \Delta\psi) - Ro^{-1}\psi_x \right) \chi^h \, d\mathbf{x}.
$$

Substituting above into (7) with the Galerkin orthogonality to the finite-element space, i.e., $a(\psi - \psi^h, \chi^h) = 0$ for all $\chi^h \in \mathcal{S}^h$, we can obtain the SQGE (1) because χ^h is arbitrary.

3.1.2. Newton–Raphson iteration

The variational formulation (7) of the problem is nonlinear. A full Newton–Raphson iteration method is employed to resolve the relevant system of equations. This involves recasting the problem as one involving a residual $\mathbf{R}$ with the form

$$
\mathbf{R}(\psi^h) = a(\psi^h, \chi^h) - \ell(\chi^h) = \mathbf{0} \quad \forall \chi^h \in \mathcal{S}^h,
\tag{20}
$$

where a and ℓ are given by (8) and (9), respectively. Given solution ψ_n^h at the nth iteration, the linearization of (20) yields an equation

$$
\mathbf{0} = \mathbf{R}(\psi_{n+1}^h, \chi^h) \simeq \mathbf{R}(\psi_n^h, \chi^h) + \left.\frac{\partial \mathbf{R}}{\partial \psi^h}\right|_n \delta\psi^h, \quad \forall \chi \in \mathcal{S}^h
\tag{21}
$$

for the increment $\delta\psi^h$ of the streamfunction ψ^h and the increment determines the solution ψ_{n+1}^h at the $(n+1)$th iteration via

$$
\psi_{n+1}^h = \psi_n^h + \delta\psi^h.
\tag{22}
$$

Additionally, the increment of $\mathbf{R}$ in (21) is given by

$$
\begin{aligned}
\frac{\partial \mathbf{R}}{\partial \psi^h}\bigg|_n \delta \psi^h &= Re^{-1} \int_{\widetilde{\Omega}} \Delta(\delta \psi^h) \Delta \chi^h \, \mathrm{d}\mathbf{x} \\
&\quad + \int_{\widetilde{\Omega}} \Delta(\delta \psi^h)((\psi_n^h)_y \chi_x^h - (\psi_n^h)_x \chi_y^h) \, \mathrm{d}\mathbf{x} + \int_{\widetilde{\Omega}} \Delta \psi_n^h ((\delta \psi^h)_y \chi_x - (\delta \psi^h)_x \chi_y) \, \mathrm{d}\mathbf{x} \\
&\quad - Re^{-1} \left(\int_{\widetilde{\Gamma}} \langle\!\langle \Delta(\delta \psi^h) \rangle\!\rangle [\![\nabla \chi^h \cdot \mathbf{n}]\!] \, \mathrm{d}s + \int_{\widetilde{\Gamma}} [\![\nabla(\delta \psi^h) \cdot \mathbf{n}]\!] \langle\!\langle \Delta \chi^h \rangle\!\rangle \, \mathrm{d}s \right) \\
&\quad + Re^{-1} \int_{\widetilde{\Gamma}} \frac{\eta}{|e|} [\![\nabla(\delta \psi^h) \cdot \mathbf{n}]\!][\![\nabla \chi^h \cdot \mathbf{n}]\!] \, \mathrm{d}s - Ro^{-1} \int_{\widetilde{\Omega}} \frac{\partial(\delta \psi^h)}{\partial x} \chi^h \, \mathrm{d}\mathbf{x}.
\end{aligned}
\tag{23}
$$

Granted the finite-element discretization, substituting (23) into (21) results in a linear system of equations,

$$
\mathbf{K}\mathbf{d} = -\mathbf{R},
\tag{24}
$$

for the increment $\mathbf{d} = (\delta \psi^h)^\top$ of the streamfunction ψ^h. In (24), the matrix $\mathbf{K}$ originates from (23) and the residual vector $\mathbf{R}$ stems from (20). Our solution strategy is to determine $\delta \psi^h$ from (24) and perform updates with (22) until convergence is attained.

3.2. Linear Stommel–Munk model

In this section, we provide a variational formulation for the linear Stommel–Munk model (Vallis [3, eqn. (14.42)]) using C^0-elements along with the coercivity analysis and the theoretical error estimate. Similar to the SQGE, the linear Stommel–Munk model also contains the biharmonic operator $\Delta^2 \psi$, the rotational term $\partial \psi / \partial x$, and the forcing term F. However, whereas the SQGE are nonlinear due to the presence of the Jacobian term $J(\psi, \Delta \psi)$, the Stommel–Munk model involves instead a Laplacian term $\Delta \psi$.

The linear Stommel–Munk model consists of the partial-differential equation

$$
-\epsilon_s \Delta \psi + \epsilon_m \Delta^2 \psi - \frac{\partial \psi}{\partial x} = F \quad \text{in } \Omega
\tag{25}
$$

and the boundary conditions (4). The parameters ϵ_s and ϵ_m are the nondimensional Stommel and Munk numbers, respectively, which are defined by

$$
\epsilon_s = \frac{\gamma}{\beta L} \quad \text{and} \quad \epsilon_m = \frac{A}{\beta L^3},
\tag{26}
$$

where γ is the coefficient of the linear drag (or Rayleigh friction), as might be generated by a bottom Ekman layer, and where β, L, and A retain the meanings introduced in connection with the SQGE (1).

For the linear Stommel–Munk model, the counterpart of the variational formulation (7) of the SQGE is: Find a streamfunction ψ^h in $\mathcal{S}^h$ such that

$$
a(\psi^h, \chi^h) = \ell(\chi^h)
\tag{27}
$$

for all test fields χ^h in $\mathcal{S}^h$, where $a(\cdot, \cdot)$ and $\ell(\cdot)$ are now defined in accord with

$$
\begin{aligned}
a(\psi^h, \chi^h) &= \epsilon_s \int_{\widetilde{\Omega}} \nabla \psi^h \cdot \nabla \chi^h \, \mathrm{d}\mathbf{x} + \epsilon_m \int_{\widetilde{\Omega}} \Delta \psi^h \Delta \chi^h \, \mathrm{d}\mathbf{x} \\
&\quad - \epsilon_m \left(\int_{\widetilde{\Gamma}} \langle\!\langle \Delta \psi^h \rangle\!\rangle [\![\nabla \chi^h \cdot \mathbf{n}]\!] \, \mathrm{d}s + \int_{\widetilde{\Gamma}} [\![\nabla \psi^h \cdot \mathbf{n}]\!] \langle\!\langle \Delta \chi^h \rangle\!\rangle \, \mathrm{d}s \right) \\
&\quad + \epsilon_m \int_{\widetilde{\Gamma}} \frac{\eta}{|e|} [\![\nabla \psi^h \cdot \mathbf{n}]\!][\![\nabla \chi^h \cdot \mathbf{n}]\!] \, \mathrm{d}s - \int_{\widetilde{\Omega}} \frac{\partial \psi^h}{\partial x} \chi^h \, \mathrm{d}\mathbf{x}
\end{aligned}
\tag{28}
$$

and

$$
\ell(\chi^h) = \int_{\widetilde{\Omega}} F \chi^h \, \mathrm{d}\mathbf{x}.
\tag{29}
$$

As with the SQGE, $\eta > 0$ represents the proportionality constant. Whereas the second term on the second line of (28) is introduced to weakly impose the flux across element boundaries, the first term on the second line imparts a variational consistency.

To analyze this model, we define the energy norm as

$$\|\psi\|_h^2 = \sum_{\Omega_i \in \widetilde{\Omega}} \left(\epsilon_s \|\nabla\psi\|_{0,\Omega_i}^2 + \epsilon_m \|\Delta\psi\|_{0,\Omega_i}^2 \right) + \sum_{e \in \widetilde{\Gamma}} \left(\epsilon_m \frac{|e|}{\eta} \|\langle\!\langle \Delta\psi \rangle\!\rangle\|_{0,e}^2 + \epsilon_m \frac{\eta}{|e|} \|[\![\nabla\psi \cdot \mathbf{n}]\!]\|_{0,e}^2 \right). \tag{30}$$

The third term in (30) can be bounded by the trace inequality

$$\sum_{e \in \widetilde{\Gamma}} \|\langle\!\langle \Delta\psi^h \rangle\!\rangle\|_{0,e}^2 \leq \sum_{\Omega_i \in \widetilde{\Omega}} \frac{1}{2} \|\Delta\psi^h\|_{0,\partial\Omega_i}^2 \leq \sum_{\Omega_i \in \widetilde{\Omega}} \frac{c_{k-2,\Omega_i}^2}{2} h_{\Omega_i}^{-1} \|\Delta\psi^h\|_{0,\Omega_i}^2 \tag{31}$$

for all $\psi^h \in \mathcal{S}^h$.

Lemma 3.3 (*Coercivity*). *Let us define* $\eta_0 = \frac{5}{4} \max_{\Omega_i \in \widetilde{\Omega}} c_{k-2,\Omega_i}^2$ *where* c_{k-2,Ω_i} *is defined in* (10). *Then, for all* $\psi^h \in \mathcal{S}^h$ *and* $\eta \geq \eta_0$, *we have*

$$a(\psi^h, \psi^h) \geq \frac{1}{2} \|\psi^h\|_h^2. \tag{32}$$

Proof. Setting $\chi^h = \psi^h$ in (28) and the trace inequality (31) yield

$$a(\psi^h, \psi^h) \geq \epsilon_s \sum_{\Omega_i \in \widetilde{\Omega}} \|\nabla\psi^h\|_{0,\Omega_i}^2 + \epsilon_m \sum_{\Omega_i \in \widetilde{\Omega}} \|\Delta\psi^h\|_{0,\Omega_i}^2$$

$$- \left| 2\epsilon_m \sum_{e \in \widetilde{\Gamma}} \|\langle\!\langle \Delta\psi^h \rangle\!\rangle\|_{0,e} \|[\![\Delta\psi^h \cdot \mathbf{n}]\!]\|_{0,e} \right| + \epsilon_m \sum_{e \in \widetilde{\Gamma}} \frac{\eta}{|e|} \|[\![\nabla\psi^h \cdot \mathbf{n}]\!]\|_{0,e}^2$$

$$\geq \epsilon_s \sum_{\Omega_i \in \widetilde{\Omega}} \|\nabla\psi^h\|_{0,\Omega_i}^2 + \frac{1}{2}\epsilon_m \sum_{\Omega_i \in \widetilde{\Omega}} \|\Delta\psi^h\|_{0,\Omega_i}^2 + 2\epsilon_m \sum_{e \in \widetilde{\Gamma}} \frac{5|e|}{4\eta_0} \|\langle\!\langle \Delta\psi^h \rangle\!\rangle\|_{0,e}^2$$

$$- 2\epsilon_m \left(\frac{1}{2\alpha} \sum_{e \in \widetilde{\Gamma}} \frac{|e|}{\eta} \|\langle\!\langle \Delta\psi^h \rangle\!\rangle\|_{0,e}^2 + \frac{\alpha}{2} \sum_{e \in \widetilde{\Gamma}} \frac{\eta}{|e|} \|[\![\nabla\psi^h \cdot \mathbf{n}]\!]\|_{0,e}^2 \right)$$

$$+ \epsilon_m \sum_{e \in \widetilde{\Gamma}} \frac{\eta}{|e|} \|[\![\nabla\psi^h \cdot \mathbf{n}]\!]\|_{0,e}^2$$

$$\geq \frac{1}{2} \sum_{\Omega_i \in \widetilde{\Omega}} \left(\epsilon_s \|\nabla\psi^h\|_{0,\Omega_i}^2 + \epsilon_m \|\Delta\psi^h\|_{0,\Omega_i}^2 \right) + 2\epsilon_m \sum_{e \in \widetilde{\Gamma}} \frac{|e|}{\eta} \left(\frac{5}{4} - \frac{1}{2\alpha} \right) \|\langle\!\langle \Delta\psi^h \rangle\!\rangle\|_{0,e}^2$$

$$+ \epsilon_m(1 - \alpha) \sum_{e \in \widetilde{\Gamma}} \frac{\eta}{|e|} \|[\![\nabla\psi^h \cdot \mathbf{n}]\!]\|_{0,e}^2.$$

To ensure the coercivity, α must satisfy $2/5 < \alpha < 1$. Then (32) holds by choosing $\alpha = 1/2$. $\square$

Similar to the SQGE, we can establish the variational consistency of (27). Let $\psi \in H^4(\Omega) \cap H_0^2(\Omega)$, then $[\![\nabla\psi \cdot \mathbf{n}]\!] = 0$. We apply integration by parts to the first term of (28) to give

$$\int_{\widetilde{\Omega}} \nabla\psi \cdot \nabla\chi^h \, \mathrm{d}v = - \int_{\widetilde{\Omega}} \Delta\psi \chi^h \, \mathrm{d}\boldsymbol{x} + \int_{\widetilde{\Gamma}} [\![(\nabla\psi \cdot \mathbf{n})\chi^h]\!] \, \mathrm{d}s$$

$$= - \int_{\widetilde{\Omega}} \Delta\psi \chi^h \, \mathrm{d}\boldsymbol{x}. \tag{33}$$

Here, we used the equality (18) and $[\![\chi^h]\!] = 0$ on $\widetilde{\Gamma}$. On substituting (17) and (33) into (27), we next find that

$$a(\psi, \chi^h) = \int_{\widetilde{\Omega}} \left(-\epsilon_s \Delta\psi + \epsilon_m \Delta^2\psi - \frac{\partial\psi}{\partial x} \right) \chi^h \, d\mathbf{x}.$$

Upon substituting above into (27) with the Galerkin orthogonality

$$a(\psi - \psi^h, \chi^h) = 0 \tag{34}$$

to the finite-element space, we can obtain the linear Stommel–Munk model (25) because χ^h can be chosen arbitrarily on $\widetilde{\Omega}$. This completes the proof of consistency for the variational formulation of the linear Stommel–Munk model.

To perform the error estimate of (27), we introduce the function space $\widetilde{\mathcal{S}}$ defined as

$$\widetilde{\mathcal{S}} := H_0^1(\Omega) \cap H^4(\Omega) = \{\psi \in H^4(\Omega) : \psi = 0 \text{ on } \partial\Omega\}. \tag{35}$$

Lemma 3.4 (*Continuity*). *For all $\psi \in \widetilde{\mathcal{S}}$, there exists a constant $C > 0$ such that*

$$a(\psi, \chi) \le C \|\|\psi\|\|_h \|\|\chi\|\|_h \quad \forall \chi \in \widetilde{\mathcal{S}}. \tag{36}$$

Proof. The Cauchy–Schwarz inequality and Poincaré–Friedrich's yield that

$$
\begin{aligned}
a(\psi, \chi) &\le \epsilon_s \sum_{\Omega_i \in \widetilde{\Omega}} \|\nabla\psi\|_{0,\Omega_i} \|\nabla\chi\|_{0,\Omega_i} + \epsilon_m \sum_{\Omega_i \in \widetilde{\Omega}} \|\Delta\psi\|_{0,\Omega_i} \|\Delta\chi\|_{0,\Omega_i} \\
&\quad + \epsilon_m \left(\sum_{e \in \widetilde{\Gamma}} \|\langle\!\langle \Delta\psi \rangle\!\rangle\|_{0,e} \|[\![\nabla\chi \cdot \mathbf{n}]\!]\|_{0,e} + \sum_{e \in \widetilde{\Gamma}} \|[\![\nabla\psi \cdot \mathbf{n}]\!]\|_{0,e} \|\langle\!\langle \Delta\chi \rangle\!\rangle\|_{0,e} \right) \\
&\quad + \epsilon_m \sum_{e \in \widetilde{\Gamma}} \frac{\eta}{|e|} \|[\![\nabla\psi \cdot \mathbf{n}]\!]\|_{0,e} \|[\![\nabla\chi \cdot \mathbf{n}]\!]\|_{0,e} + \sum_{\Omega_i \in \widetilde{\Omega}} \|\partial\psi/\partial x\|_{0,\Omega_i} \|\chi\|_{0,\Omega_i} \\
&\le \left(\epsilon_s \|\nabla\psi\|_{0,\widetilde{\Omega}}^2 \right)^{\frac{1}{2}} \left(\epsilon_s \|\nabla\chi\|_{0,\widetilde{\Omega}}^2 \right)^{\frac{1}{2}} + \left(\epsilon_m \|\Delta\psi\|_{0,\widetilde{\Omega}}^2 \right)^{\frac{1}{2}} \left(\epsilon_m \|\Delta\chi\|_{0,\widetilde{\Omega}}^2 \right)^{\frac{1}{2}} \\
&\quad + \left(\epsilon_m \sum_{e \in \widetilde{\Gamma}} \frac{|e|}{\eta} \|\langle\!\langle \Delta\psi \rangle\!\rangle\|_{0,e}^2 \right)^{\frac{1}{2}} \left(\epsilon_m \sum_{e \in \widetilde{\Gamma}} \frac{\eta}{|e|} \|[\![\nabla\chi \cdot \mathbf{n}]\!]\|_{0,e}^2 \right)^{\frac{1}{2}} \\
&\quad + \left(\epsilon_m \sum_{e \in \widetilde{\Gamma}} \frac{\eta}{|e|} \|[\![\nabla\psi \cdot \mathbf{n}]\!]\|_{0,e}^2 \right)^{\frac{1}{2}} \left(\epsilon_m \sum_{e \in \widetilde{\Gamma}} \frac{|e|}{\eta} \|\langle\!\langle \Delta\chi \rangle\!\rangle\|_{0,e}^2 \right)^{\frac{1}{2}} \\
&\quad + \left(\epsilon_m \sum_{e \in \widetilde{\Gamma}} \frac{\eta}{|e|} \|[\![\nabla\psi \cdot \mathbf{n}]\!]\|_{0,e}^2 \right)^{\frac{1}{2}} \left(\epsilon_m \sum_{e \in \widetilde{\Gamma}} \frac{\eta}{|e|} \|[\![\nabla\chi \cdot \mathbf{n}]\!]\|_{0,e}^2 \right)^{\frac{1}{2}} \\
&\quad + \epsilon_s^{-1} C_{P,\Omega} h_\Omega \left(\epsilon_s \|\nabla\psi\|_{0,\widetilde{\Omega}}^2 \right)^{\frac{1}{2}} \left(\epsilon_s \|\nabla\chi\|_{0,\widetilde{\Omega}}^2 \right)^{\frac{1}{2}} \\
&\le C \|\|\psi\|\|_h \|\|\chi\|\|_h
\end{aligned}
$$

where $C \ge \max\{1 + c, \sqrt{2(1 + c)}, \sqrt{3}\}$, $c = \epsilon_s^{-1} C_{P,\Omega} h_\Omega$ and $C_{P,\Omega}$ is the Poincaré constant in Ω. $\square$

In the following theorems, we provide the error estimates in the energy norm and the L^2-norm. We first begin by deriving the error estimate in the energy norm.

Theorem 3.5. *Suppose $\psi \in H^{k+1}(\Omega)$ be the solution of (25) and $\psi^h \in \mathcal{S}^h$ satisfies (27) for all $\chi^h \in \mathcal{S}^h$. Then*

$$\|\|\psi - \psi^h\|\|_h \le ch^{k-1} \|\psi\|_{k+1,\Omega}. \tag{37}$$

Proof. Let $\mathcal{I}_h\psi$ be the continuous interpolant of ψ. Then the triangle inequality yields

$$\|\psi - \psi^h\|_h \leq \|\psi - \mathcal{I}_h\psi\|_h + \|\mathcal{I}_h\psi - \psi^h\|_h. \tag{38}$$

Galerkin orthogonality (34), the coercivity (32), and the continuity (36) lead to

$$\frac{1}{2}\|\psi^h - \mathcal{I}_h\psi\|_h^2 \leq a(\psi^h - \mathcal{I}_h\psi, \psi^h - \mathcal{I}_h\psi) = a(\psi - \mathcal{I}_h\psi, \psi^h - \mathcal{I}_h\psi)$$

$$\leq C\|\psi - \mathcal{I}_h\psi\|_h\|\psi^h - \mathcal{I}_h\psi\|_h.$$

Then, we obtain the following inequality

$$\|\psi^h - \mathcal{I}_h\psi\|_h \leq 2C\|\psi - \mathcal{I}_h\psi\|_h. \tag{39}$$

Applying above inequality to (38) gives rise to

$$\|\psi - \psi^h\|_h \leq (1 + 2C)\|\psi - \mathcal{I}_h\psi\|_h. \tag{40}$$

From the definition of the energy norm (30), we obtain

$$\|\psi - \mathcal{I}_h\psi\|_h^2 = \sum_{\Omega_i \in \widetilde{\Omega}} \left(\epsilon_{\mathrm{s}}\|\nabla(\psi - \mathcal{I}_h\psi)\|_{0,\Omega_i}^2 + \epsilon_{\mathrm{m}}\|\Delta(\psi - \mathcal{I}_h\psi)\|_{0,\Omega_i}^2 \right)$$

$$+ \sum_{e \in \widetilde{\Gamma}} \left(\epsilon_{\mathrm{m}}\frac{|e|}{\eta}\|\langle\!\langle \Delta(\psi - \mathcal{I}_h\psi)\rangle\!\rangle\|_{0,e}^2 + \epsilon_{\mathrm{m}}\frac{\eta}{|e|}\|[\![\nabla(\psi - \mathcal{I}_h\psi)\cdot\mathbf{n}]\!]\|_{0,e}^2 \right). \tag{41}$$

Bearing in mind that the interpolation error estimate yields the inequalities

$$\|\nabla(\psi - \mathcal{I}_h\psi)\|_{0,\Omega_i}^2 \leq c_i^2 h_{\Omega_i}^{2k}\|\psi\|_{k+1,\Omega_i}^2,$$

$$\|\Delta(\psi - \mathcal{I}_h\psi)\|_{0,\Omega_i}^2 \leq c_i^2 h_{\Omega_i}^{2k-2}\|\psi\|_{k+1,\Omega_i}^2,$$

and the trace inequality [30] yields

$$\|\psi\|_{0,\partial\Omega_i}^2 \leq c_t\left(h_{\Omega_i}^{-1}\|\psi\|_{0,\Omega_i}^2 + h_{\Omega_i}|\psi|_{1,\Omega_i} \right) \quad \forall\psi \in H^1(\Omega_i),$$

we can obtain additional inequalities

$$h_{\Omega_i}\|\Delta(\psi - \mathcal{I}_h\psi)\|_{0,\partial\Omega_i}^2 \leq c_t h_{\Omega_i}\left(h_{\Omega_i}^{-1}\|\Delta(\psi - \mathcal{I}_h\psi)\|_{0,\Omega_i}^2 + h_{\Omega_i}|\Delta(\psi - \mathcal{I}_h\psi)|_{1,\Omega_i}^2 \right)$$

$$\leq c_t\left(c_i^2 h_{\Omega_i}^{2k-2}\|\psi\|_{k+1,\Omega_i}^2 + h_{\Omega_i}^2 c_i^2 h_{\Omega_i}^{2k-4}\|\psi\|_{k+1,\Omega}^2 \right)$$

$$= 2c_t c_i^2 h_{\Omega_i}^{2k-2}\|\psi\|_{k+1,\Omega_i}^2,$$

$$h_{\Omega_i}^{-1}\|\nabla(\psi - \mathcal{I}_h\psi)\cdot\boldsymbol{n}\|_{0,\partial\Omega_i}^2 \leq c_t h_{\Omega_i}^{-1}\left(h_{\Omega_i}^{-1}|\psi - \mathcal{I}_h\psi|_{1,\Omega_i}^2 + h_{\Omega_i}|\psi - \mathcal{I}_h\psi|_{2,\Omega_i}^2 \right)$$

$$\leq c_t\left(h_{\Omega_i}^{-2}c_i^2 h_{\Omega_i}^{2k}\|\psi\|_{k+1,\Omega}^2 + c_i^2 h_{\Omega_i}^{2k-2}\|\psi\|_{k+1,\Omega_i}^2 \right)$$

$$= 2c_t c_i^2 h_{\Omega_i}^{2k-2}\|\psi\|_{k+1,\Omega_i}^2.$$

Applying above inequalities to (41) leads to (37).

In the following theorem, we derive the error estimate in the L^2-norm.

Theorem 3.6. *Suppose $\psi \in H^{k+1}(\Omega)$ be the solution of* (25) *and $\psi^h \in \mathcal{S}^h$ satisfies* (27) *for all $\chi^h \in \mathcal{S}^h$. Then*

$$\|\psi - \psi^h\|_{0,\Omega} \leq ch^{k+1}\|\psi\|_{k+1,\Omega} \tag{42}$$

for $k \geq 3$ and

$$\|\psi - \psi^h\|_{0,\Omega} \leq ch^k\|\psi\|_{k+1,\Omega} \tag{43}$$

for $k = 2$.

Proof. Consider the dual problem with homogeneous boundary conditions which involves: Find $\phi \in \mathcal{S}$ such that

$$B(\phi, \chi) = \int_{\widetilde{\Omega}} (\psi - \psi^h) \chi \; \mathrm{d}\boldsymbol{x} \quad \forall \chi \in \mathcal{S}. \tag{44}$$

with the elliptic regularity estimate

$$\|\phi\|_{4,\Omega} \le c_r \|\psi - \psi^h\|_{0,\Omega}. \tag{45}$$

In (44), by setting $\chi = \psi - \psi^h$ and using the continuity (36) and the Galerkin orthogonality (34), we obtain

$$
\begin{aligned}
\|\psi - \psi^h\|_{0,\Omega}^2 &= B(\phi, \psi - \psi^h) \\
&= B(\phi - \phi^h, \psi - \psi^h) + B(\phi^h, \psi - \psi^h) \\
&= B(\phi - \phi^h, \psi - \psi^h) \\
&\le C \|\!|\phi - \phi^h|\!\|_h \|\!|\psi - \psi^h|\!\|_h.
\end{aligned} \tag{46}
$$

If we consider ϕ^h as the finite-element solution to the dual problem, it follows from (37) that

$$\|\!|\phi - \phi^h|\!\|_h \le ch^2 \|\phi\|_{4,\Omega} \tag{47}$$

for $k \ge 3$ and

$$\|\!|\phi - \phi^h|\!\|_h \le ch \|\phi\|_{4,\Omega} \tag{48}$$

for $k = 2$. For $k \ge 3$, applying (37) and (47) into (46) yields

$$\|\psi - \psi^h\|_{0,\Omega}^2 \le Ch^{k+1} \|\phi\|_{4,\Omega} \|\psi\|_{k+1,\Omega}.$$

Then the elliptic regularity estimate (45) leads

$$\|\psi - \psi^h\|_{0,\Omega}^2 \le c_r Ch^{k+1} \|\psi - \psi^h\|_{0,\Omega} \|\psi\|_{k+1,\Omega}.$$

As a result, (42) is obtained for $k \ge 3$. For $k = 2$, similar steps using (48) instead of (47) yield

$$\|\psi - \psi^h\|_{0,\Omega}^2 \le c_r Ch^k \|\psi - \psi^h\|_{0,\Omega} \|\psi\|_{k+1,\Omega}.$$

This completes the proof of (43) for $k = 2$. $\square$

Notice that the convergence rate in the L^2-norm is quadratic for $k = 2$.

3.3. Linear Stommel model

In this section, we introduce the linear Stommel model (Vallis [3, eqn. (14.22)]) which is a simplified version of the SQGE commonly used for the large scale wind-driven ocean circulation. In contrast to the previously considered models, this one involves a second-order PDE involving a Laplacian term, a rotational term, and a forcing term. Moreover, only the Dirichlet condition is imposed on the boundary. Specifically, the linear Stommel model is given by

$$\left. \begin{aligned} -\epsilon_s \Delta \psi - \frac{\partial \psi}{\partial x} &= F \quad \text{in } \Omega, \\ \psi &= 0 \quad \text{on } \Gamma, \end{aligned} \right\} \tag{49}$$

where ϵ_s is the Stommel number defined in (26)$_1$. Notice that the Stommel model can be scaled by dividing through by ϵ_s. In this case, this model is similar to the SQGE. Furthermore, ϵ_s can be identified with Ro.

Since the PDE entering (49) is of second-order, all admissible solution and test fields belong to the Sobolev space $\mathcal{S} = H^1(\Omega)$ of functions defined on Ω that are square-integrable and have square-integrable first derivatives. The variational form of this model can be obtained by taking $\epsilon_m = 0$ in (27). Since this is second-order, Nitsche's formulation is not required. However, convergence studies are performed to verify accuracy of our algorithm.
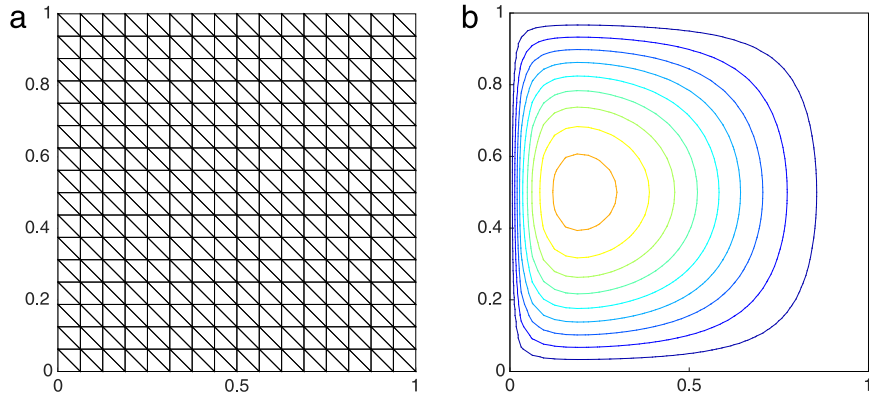
Fig. 1. The Stommel model: (a) A finite-element mesh model with triangular elements and (b) streamlines of the approximation to the solution on a mesh size of $h = 1/16$.

4. Numerical studies

To verify Nitsche-type variational formulations for the SQGE and the linear Stommel–Munk model, we perform numerical studies on several benchmark problems commonly used (see, for example, Vallis [3]) in geophysical fluid dynamics. Specifically, we provide convergence studies using C^0 basis functions on triangular elements. We do not provide error estimates for our variational formations. However, on the basis of an analysis of similar variational formulations obtained by Foster et al. [10], we expect that the optimal rates of convergence of a finite-element discretization using basis functions with the order k are respectively $k + 1$, k, and $k - 1$ in the L^2-, H^1-, and H^2-norms. Our numerical studies focus on determining whether the optimal rates of convergence can be obtained with the variational formulations proposed in the previous section. For this purpose, unless otherwise specified, we denote the errors in L^2-norm, H^1-seminorm, and H^2-seminorm by $\|\psi - \psi^h\|_{0,h}$, $|\psi - \psi^h|_{1,h}$, and $|\psi - \psi^h|_{2,h}$, respectively, in the plots of the convergence history. Moreover, convergence studies for all simulations are performed using the standard Lagrange polynomial basis functions of degrees $k = 2$ and $k = 3$.

The performance of the variational formulations derived in the previous section is sensitive to the chosen values of the proportionality constant η. From the coercivity analyses for both SQGE and Stommel–Munk model, the optimal proportionality constant η must be larger than or equal to η_0 with $\eta_0 = 2 \max_{\Omega_i \in \tilde{\Omega}} c_{k-2,\Omega_i}^2$, where c_{k-2,Ω_i} is defined as (10). Unless otherwise indicated, all simulations in this study are performed by taking $\eta = \eta_0$. Our numerical results show the robustness of the method for $\eta \geq \eta_0$.

4.1. Linear Stommel model

As mentioned in Section 3.3, the Stommel model is a second-order PDE which requires C^0-basis functions. Thus, a Nitsche's type formulation for this model is not required. It is worth emphasizing that the variational form of this model can be obtained by taking $\epsilon_m = 0$ in (27). However, we provide numerical results to verify capability of our algorithm to the ocean circulation simulation using the Stommel model.

Our study is performed using the exact solution

$$\psi(x, y) = \frac{\sin(\pi y)}{\pi(1 + 4\pi^2\epsilon_s^2)}\{2\pi\epsilon_s \sin(\pi x) + \cos(\pi x) + [(1 + e^{R_2})e^{R_1 x} - (1 + e^{R_1})e^{R_2 x}]/(e^{R_1} - e^{R_2})\} \qquad (50)$$

over the domain $\Omega = [0, 1] \times [0, 1]$. In (50), R_1 and R_2 are given by

$$R_1 = \frac{-1 + \sqrt{1 + 4\pi^2\epsilon_s^2}}{2\epsilon_s} \quad \text{and} \quad R_2 = \frac{-1 - \sqrt{1 + 4\pi^2\epsilon_s^2}}{2\epsilon_s}.$$

This solution was used by Myers and Weaver [37] and Foster et al. [10]. By taking the Stommel number to obey $\epsilon_s = 0.05$, we work in a setting identical to that considered in these references. The forcing term F is chosen to match that given by the exact solution (50). A computational domain shown in Fig. 1 can be considered as a rectangular
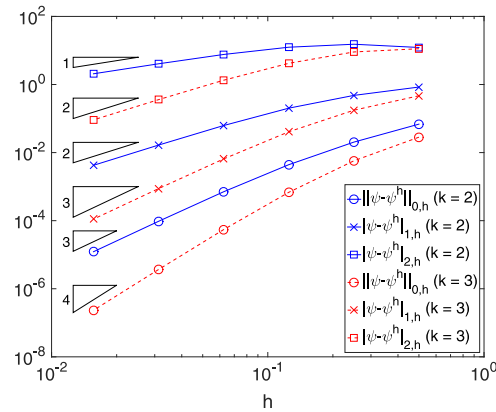
Fig. 2. The Stommel model: Convergence history of the test problem (50) for $k = 2$ and $k = 3$.
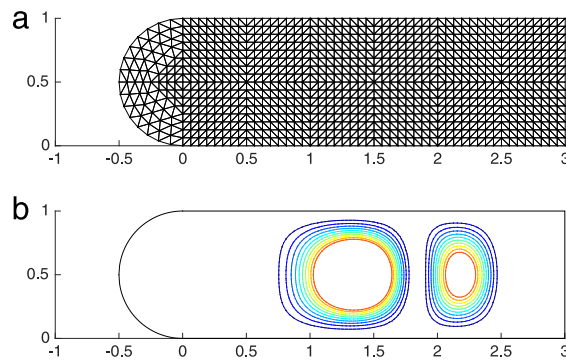

Fig. 3. The Stommel model: (a) A finite-element mesh model with a mesh size of $h = 1/16$ and (b) streamlines of the approximation to the solution for a domain with one-side curved boundary.

ocean. With the origin of a cartesian coordinate system at the southwest corner, the x- and y-axis point eastward and northward, respectively, and the boundaries of the computational domain are the shores of the ocean.

Fig. 1(a) displays a finite-element mesh model with triangular elements used in our simulation. Fig. 1(b) shows the streamlines of the approximation to the solution obtained using a mesh size of $h = 1/16$. This numerical solution is consistent with one obtained by Myers and Weaver [37] and Foster et al. [10]. In particular, as is evident from the figure, it exhibits a thin western boundary layer. Fig. 2 shows the convergence rates in the L^2-norm, the H^1-seminorm, and the H^2-seminorm for Lagrange polynomial basis functions of orders $k = 2$ and 3. Optimal rates of convergence for both $k = 2$ and $k = 3$ are obtained for all three norms. Slightly lower rates of convergence are obtained on coarse mesh due to the presence of the strong western boundary layer, as just the work in Foster et al. [10].

Next, we consider an ocean shape with a western semicircle boundary as shown in Fig. 3. Our study is performed using the exact solution

$$\psi(x, y) = \sin^2(x^2 + (y - 1/2)^2 - 1/4) \sin^2(\pi x/3) \sin^2(\pi y) \tag{51}$$

over the domain. The forcing term F is chosen to match that given by the exact solution (51). The finite-element mesh model used in this test problem is displayed in Fig. 3(a) for a mesh size of $h = 1/16$. Here, triangular elements are fitted into the curved boundary. The streamlines of the approximation to the solution are shown in Fig. 3(b). Using the exact solution (51), we check the $(k + 1)$th order convergence in the L^2-norm, the kth order convergence in the H^1-seminorm, and the $(k - 1)$th order convergence in the H^2-seminorm for $k = 2$ and 3. As shown in Fig. 4, the optimal rates of convergence are obtained for all three norms. These results indicate the accuracy and robustness of our finite-element algorithm for the large scale wind-driven ocean circulation using the Stommel model on rectangular and curved geometries.
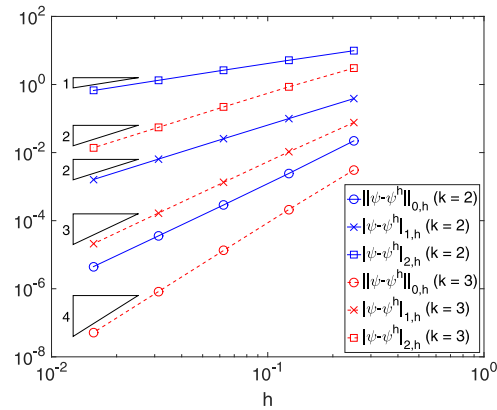
Fig. 4. The Stommel model: Convergence history for a domain with one-side curved boundary.

4.2. Linear Stommel–Munk model

In this section, we present a numerical investigation for the Stommel–Munk model. In contrast to the Stommel model, the Stommel–Munk model involves a fourth-order term and, thus, requires C^1-continuous basis functions to achieve a conforming finite-element discretization. We consider a nonconforming finite-element algorithm using the Nitsche-type variational formulation (27). Numerical studies are performed using C^0-continuous basis functions with orders of $k = 2$ and 3.

Our study uses two test problems with exact solutions

$$\psi(x, y) = \sin^2(\pi x/3) \sin^2(\pi y) \quad \text{in } \Omega = [0, 3] \times [0, 1] \tag{52}$$

and

$$\psi(x, y) = [(1 - x/3)(1 - e^{-20x}) \sin(\pi y)]^2 \quad \text{in } \Omega = [0, 3] \times [0, 1]. \tag{53}$$

These solutions were used to test a finite-element algorithm for large-scale ocean circulation problems by Cascón et al. [38] and Foster et al. [10]. We use conditions identical to those employed in these references by taking the Munk number $\epsilon_m = 6 \times 10^{-5}$ and the Stommel number $\epsilon_s = 0.05$. The forcing term F is chosen to match those determined by the exact solutions (52) and (53).

Fig. 5 displays the streamlines of the approximations to the exact solutions (52) and (53). Fig. 5(a) shows the test problem (53) that exhibits a thin boundary layer, in the vicinity of $x = 0$, corresponding to a western boundary layer. Fig. 5(b) shows the test problem (52) that does not display a boundary layer. Notice that the finite-element mesh model used for these test problems is similar to the model in Fig. 1(a).

In Fig. 6, we display convergence history for these two test problems. Similar to the Stommel model, we obtain the order $(k + 1)$th convergence in the L^2-norm, the order kth convergence in the H^1-seminorm, and the order $(k - 1)$th convergence in the H^2-seminorm, respectively, for $k = 3$. Due to the presence of the western boundary layer, slightly lower convergence rates are obtained for the test problem (53) on coarse mesh as shown in Fig. 6(b). Moreover, the errors for the test problem (53) are relatively larger than those for the test problem (52). For $k = 2$, the rates of convergence in both H^1- and H^2-seminorms are optimal, and the quadratic rate of convergence in the L^2-norm is observed as predicted. Indeed, quadratic convergence in the L^2-norm can be established via a duality argument and Galerkin orthogonality, which will appear elsewhere.

We next study the capability of our algorithm to the domain with a curved boundary as shown in Fig. 3. Similar to the Stommel model, our study is performed using the exact solution (51). The forcing term F is computed by substituting the exact solution (51) to the Stommel–Munk model (25).

Fig. 7 shows the convergence history for the approximation to the solution (51). We observe the optimal rates of convergence in the L^2-norm, the H^1-seminorm, and the H^2-seminorm for $k = 3$. Similar to the previous example, whereas the rates in the H^1- and H^2-seminorms are optimal for $k = 2$, the quadratic convergence in the L^2-norm is obtained. These results indicate that our algorithm using cubic basis functions is more accurate and robust than quadratic basis functions.
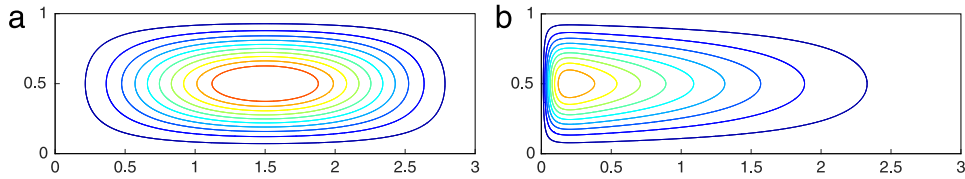
Fig. 5. The Stommel–Munk model: Streamlines of the approximation to the solutions (a) (52) without any thin boundary layer and (b) (53) with a strong western boundary layer.
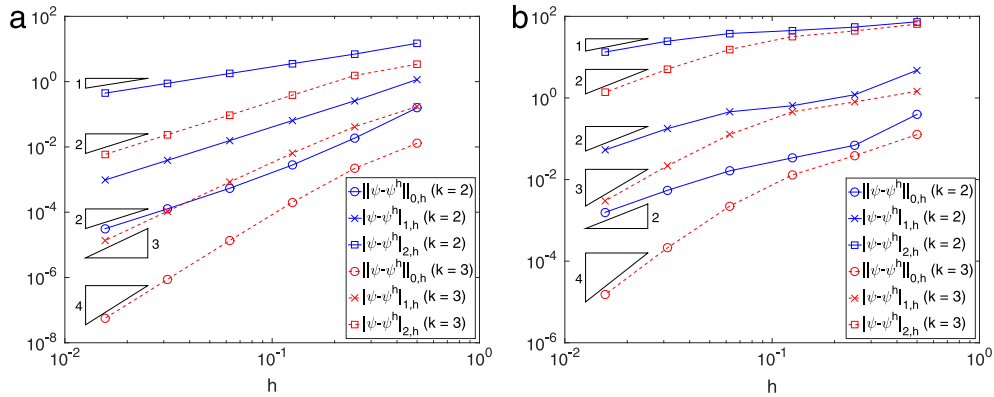

Fig. 6. The Stommel–Munk model: Convergence history for the test problems (a) (52) without any thin boundary layer and (b) (53) with a strong western boundary layer.
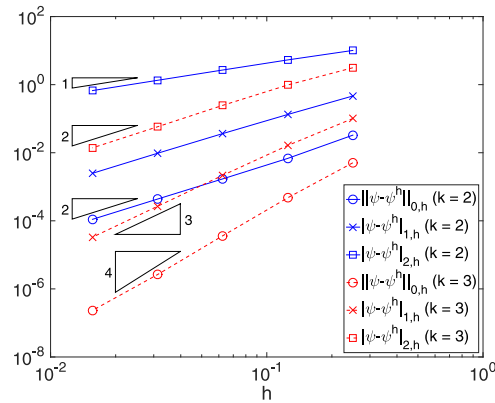

Fig. 7. The Stommel–Munk model: Convergence history for a domain with one-side curved boundary.

4.3. Stationary quasi-geostrophic equations

This section presents a numerical study for the variational formulation (7) of the SQGE. In contrast to the previous two linear models, the SQGE are nonlinear and, thus, requires a nonlinear solver. We employ the Newton–Raphson iteration method described in Section 3.1.2 and use $\psi = 0$ as an initial guess. We use the maximum norm of $\delta\psi^h$, $\|\delta\psi^h\|_\infty$, of 10^{-8} as the stopping criteria for the nonlinear solver.

We study two test problems (52) and (53), corresponding to the solutions given in Tests 1 and 2 of Cascón et al. [38] and Tests 5 and 6 of Foster et al. [10]. We consider the same setting with these references by taking the Reynolds number $Re = 1.667$ and the Rossby number $Ro = 10^{-4}$. The streamlines of the numerical solutions for two examples are not displayed in the present study. However, we note that they are indistinguishable from the exact solutions shown in Fig. 5 and are similar to numerical solutions obtained by Cascón et al. [38] and Foster et al. [10].

In Fig. 8, we monitor the convergence history in the L^2-norm, the H^1-seminorm, and the H^2-seminorm for $k = 2$ and 3. We obtain the order $(k+1)$th convergence in the L^2-norm, the order kth convergence in the H^1-seminorm,
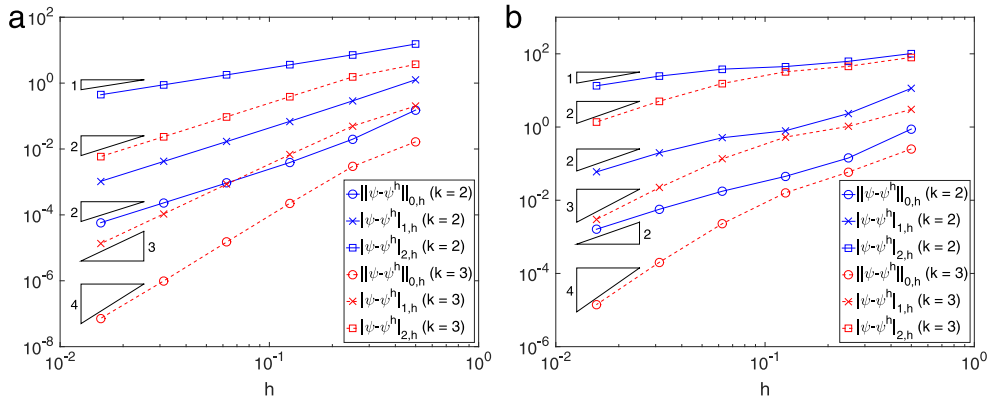
Fig. 8. The SQGE: Convergence history for the test problems (a) (52) without any thin boundary layer and (b) (53) with a strong western boundary layer.

and the order $(k-1)$th convergence in the H^2-seminorm, respectively. Quadratic convergence rates in the L^2-norm are observed for $k = 2$ as in the previous section, indicating higher accuracy and robustness of cubic basis functions than quadratic basis functions. Similar to the linear Stommel–Munk model, we have good convergence rates with the presence of the strong western boundary layer. In Fig. 9, we display the sensitivity of the errors in all three norms with respect to the parameter η for the test problem (53) with a western boundary layer. Plots are provided for $k = 3$ and three cases of η, i.e., $\eta = \eta_0$, $2\eta_0$, and $3\eta_0$ where $\eta_0 = 2 \max_{\Omega_i \in \widetilde{\Omega}} c^2_{k-2,\Omega_i}$ obtained from coercivity Theorem 3.2 of the SQGE. Optimal rates of convergence are observed for all three values of η, indicating that the variational formulation (7) is less sensitive to the parameter η. These results show that our algorithm is accurate and robust with the choice of η from the coercivity analysis. We do not display the sensitivity of the errors for $k = 2$. However, we note that it is similar to the sensitivity of the errors for $k = 3$.

We next investigate the convergence rate for the domain with one-side curved boundary as shown in Fig. 3. Fig. 10 shows the convergence history for the approximation to the solution (51). The convergence rates of this model are similar to those of the Stommel–Munk model. These results verify the accuracy and robustness of our algorithm on both rectangular and curved domains for the large scale ocean circulation simulations using the SQGE.

Motivated by above convergence studies, we investigate the capability of our algorithm to a more realistic example using the forcing term from the derivative of the wind stress (Myers and Weaver [37]). Notice that analytical solutions are not available so that convergence studies cannot be performed. We apply our method to the Mediterranean sea example with complex coastlines which was studied by Foster et al. [10]. The shape of the geometry and one example of the finite-element mesh models used in this simulation are displayed in Fig. 11. The actual coastline of the Mediterranean sea is simplified by a polygon with 35 vertices. The finite-element mesh model shown in the figure has the number of elements 4480 with total degrees of freedom 8633 for $k = 2$ and 19,669 for $k = 3$.

To compare our simulation result with Foster et al. [10], we choose the same setting with the reference, i.e., a forcing term $F = \sin(\pi x/4)$, the Reynolds number $Re = 5.27$, and the Rossby number $Ro = 6.051 \times 10^{-4}$. Fig. 12 shows the streamlines of the approximate solution for $k = 2$ with total degrees of freedom 8633. The streamfunction plot is qualitatively similar to the plot in Fig. 6 obtained by Foster et al. [10] using the Argyris element on the fine mesh with 955,302 degrees of freedom. This result indicates that our method can accurately and efficiently approximate the real ocean circulation with complex coastlines.

5. Comparison with B-splines

In this section, we study the efficiency and accuracy of our method along with the B-spline based finite-element method introduced by Kim et al. [11]. This study is performed for the SQGE using the test problem (53) with the western boundary layer. Due to the difference in algorithm, an exact comparison between two methods is a challenging task. For easy comparison, both methods are implemented in MATLAB and use the third-order basis functions. We use the same stopping criteria as described in Foster et al. [10] and the computer with CPU of Intel(R) core(TM) i5-4690 3.50 GHz and RAM 8 GB.
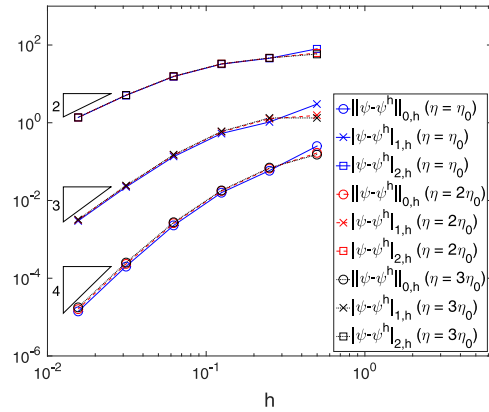
Fig. 9. The SQGE: Sensitivity of the convergence history to the variation of η for the test problem (53) with a western boundary layer for $k = 3$.
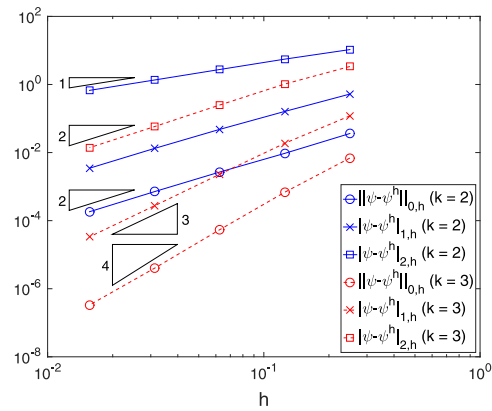

Fig. 10. The SQGE: Convergence history for a domain with one-side curved boundary.

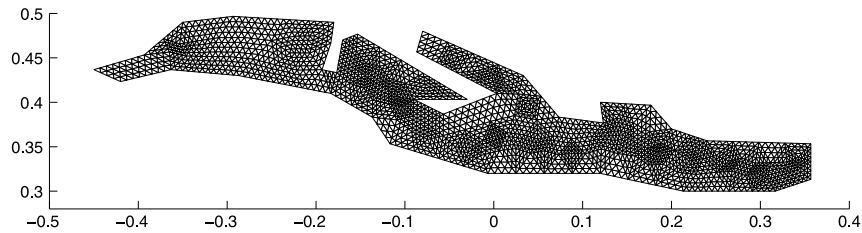

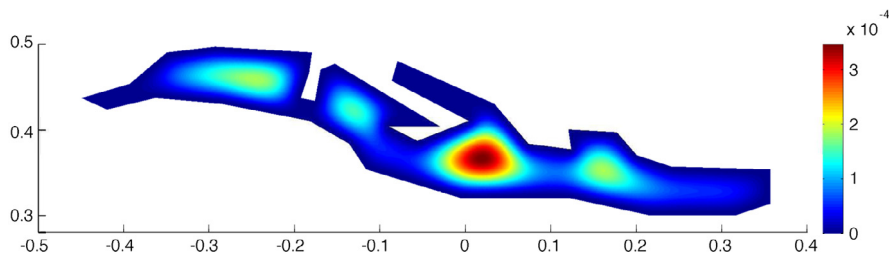Fig. 11. The finite-element mesh model with total degrees of freedom 8633 for $k = 2$ and 19,669 for $k = 3$.

Fig. 12. The SQGE: Streamlines of the numerical solution for the Mediterranean sea obtained using the mesh in Fig. 11 for $k = 2$.
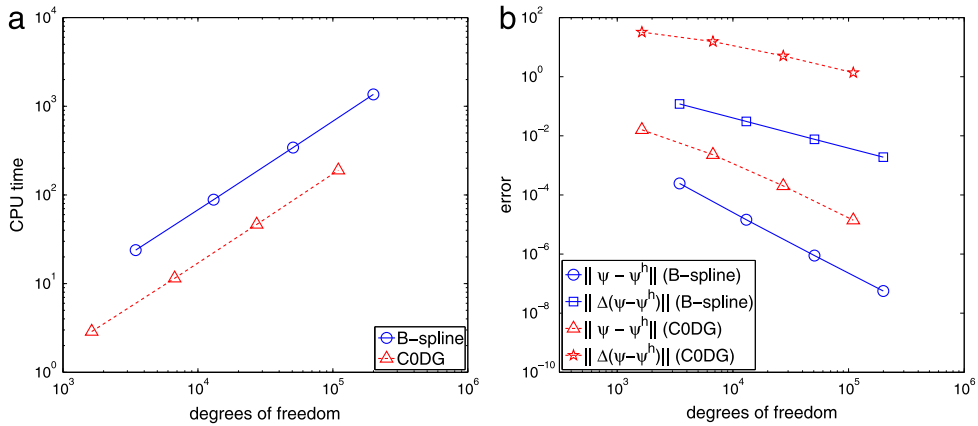
Fig. 13. Comparison between B-spline (Kim et al. [11]) and the proposed method with respect to (a) CPU time and (b) error.

In Fig. 13, we display the CPU time and the errors with respect to the degrees of freedom. The results for four cases of the degrees of freedom corresponding to the mesh size of $h = 1/8$, $1/16$, $1/32$, and $1/64$ for the proposed method and $h = 1/32$, $1/64$, $1/128$, and $1/256$ for B-splines are provided. In contrast to the standard third-order basis functions used in the proposed method, the support of the cubic B-splines is defined over the interval $4h$ where h is the mesh size as shown in Figure 5 of Höllig [13] and Figure 1 of Kim et al. [11]. As a consequence, it is not easy to compare both methods at the same degrees of freedom. Due to the smaller mesh size, while B-splines are more accurate than the proposed method at the similar number of degrees of freedom as shown in panel (b) of the figure, the convergence behaviors for both methods are similar. On the other hand, the CPU time of the proposed method is lower than that of B-splines as shown in panel (a) of the figure. This indicates that the proposed C^0-discontinuous Galerkin method with the third-order basis functions can be more efficient than cubic B-splines.

6. Conclusion

In this paper, we introduced a finite-element method using C^0 basis functions for the streamfunction formulation of the SQGE. We used Nitsche's method to weakly impose continuity of the first derivatives across element interfaces. Variational consistency of the method was verified. In addition to the SQGE, we provided the Nitsche-type formulation for the linear Stommel–Munk model which is the standard simplified version of the SQGE used in geophysical fluid dynamics. The proposed variational formulations involve the stabilization term with a proportionality constant which influences both convergence rates and the numerical accuracy. We used a coercivity analysis to determine values of this proportionality constant.

Our algorithm was first verified using numerical examples with and without a thin boundary layer on a rectangular domain. While optimal convergence rates were obtained for the example without the thin boundary layer, slightly lower convergence rates were observed on the coarse mesh but the optimal convergence rates were recovered on the fine mesh for the example with the strong western boundary layer. These convergence behaviors are similar to those obtained using Argyris elements by Foster et al. [10] and B-splines by Kim et al. [11]. Moreover, optimal rates of convergence were obtained for the domain with a one-side curved boundary. These results indicate that the proposed finite-element method can capture a thin boundary layer as well as arbitrary shaped coastal boundaries with good accuracy. Rather than using C^0 quadratic basis functions, the algorithm using C^0 cubic basis functions is more robust and accurate. We also applied our algorithm to the Mediterranean sea example with the wind forcing and obtained the qualitatively similar numerical solution with Foster et al. [10], demonstrating the capability of our algorithm to the ocean circulation simulation.

In the future, we will perform the theoretical error estimate for the variational formulation of the SQGE. Furthermore, *a posteriori* error estimate will be developed to capture more efficiently and accurately a thin western boundary layer. Finally, we intend to extend this study to the time-dependent QGE and the two-layer QGE.

Acknowledgment

References

[1] H.A. Dijkstra, Nonlinear Physical Oceanography: A Dynamical Systems Approach to the Large Scale Ocean Circulation and El Niño, Springer-Verlag, 2005.

[2] M. Ghil, M.D. Chekroun, E. Simonnet, Climate dynamics and fluid mechanics: Natural variability and related uncertainties, Physica D 237 (2008) 2111–2126.

[3] G.K. Vallis, Atmosphere and Ccean Fluid Dynamics: Fundamentals and Large-Scale Circulation, Cambridge University Press, 2006.

[4] B. Cushman-Roisin, J.M. Beckers, Introduction to Geophysical Fluid Dynamics: Physical and Numerical Aspects, Academic Press, 2011.

[5] A. Majda, Introduction to PDEs and Waves for the Atmosphere and Ocean, AMS, New York, 2003.

[6] A. Majda, X. Wang, Nonlinear Dynamics and Statistical Theories for Basic Geophysical Flows, Cambridge University Press, 2006.

[7] J. Pedlosky, Geophysical Fluid Dynamics, Springer-Verlag, 1992.

[8] J. McWilliams, Fundamentals of Geophysical Fluid Dynamics, Cambridge University Press, 2006.

[9] G.J. Fix, Finite element models for ocean circulation problems, SIAM J. Appl. Math. 29 (3) (1975) 371–387.

[10] E.L. Foster, T. Iliescu, Z. Wang, A finite element discretization of the streamfunction formulation of the stationary quasi-geostrophic equations of the ocean, Comput. Methods Appl. Mech. Engrg. 261 (2013) 105–117.

[11] T.-Y. Kim, T. Iliescu, E. Fried, B-spline based finite-element method for the stationary quasi-geostrophic equations of the ocean, Comput. Methods Appl. Mech. Engrg. 286 (2015) 168–191.

[12] W. Jiang, T.-Y. Kim, Spline-based finite-element method for the stationary quasi-geostrophic equations on arbitrary shaped coastal boundaries, Comput. Methods Appl. Mech. Engrg. (2015) http://dx.doi.org/10.1016/j.cma.2015.11.003, in press.

[13] K. Höllig, Finite Element Methods with B-Splines, SIAM, Philadelphia, 2003.

[14] J.A. Nitsche, Über ein Variationsprinzip zur Lösung von Dirichlet-Problemen bei Verwendung von Teilräumen, die keinen Randbedingungen unterworfen sind, Abh. Math. Semin. Univ. Hambg., 1970/71, 36, pp. 9–15.

[15] G. Engel, K. Garikipati, T.J.R. Hughes, M.G. Larson, L. Mazzei, R.L. Taylor, Continuous/discontinuous finite element approximations of fourth-order elliptic problems in structural and continuum mechanics with applications to thin beams and plates, and strain gradient elasticity, Comput. Methods Appl. Mech. Engrg. 191 (2002) 3669–3750.

[16] S.C. Brenner, L. Sung, C^0 interior penalty methods for fourth order elliptic boundary value problems on polygonal domain, J. Sci. Comput. 22–23 (1–3) (2005) 83–118.

[17] S.C. Brenner, M. Neilan, L.-Y. Sung, Isoparametric C^0 interior penalty methods for plate bending problems on smooth domains, Calcolo 50 (1) (2013) 35–67.

[18] G.N. Wells, N.T. Dung, A C0 discontinuous Galerkin formulation for Kirchhoff plates, Comput. Methods Appl. Mech. Engrg. 196 (35–36) (2007) 3370–3380.

[19] P. Hansbo, D. Heintz, M.G. Larson, A finite element method with discontinuous rotations for the Mindlin-Reissner plate model, Comput. Methods Appl. Mech. Engrg. 200 (5–8) (2011) 638–648.

[20] G.A. Baker, Finite element methods for elliptic equations using nonconforming elements, Math. Comp. 31 (137) (1977) 45–59.

[21] A. Embar, J. Dolbow, I. Harari, Imposing Dirichlet boundary conditions with Nitsche's method and spline-based finite elements, Internat. J. Numer. Methods Engrg. 83 (2010) 877–898.

[22] A. Embar, J. Dolbow, E. Fried, Microdomain evolution on giant unilamellar vesicles, Biomechanics and Modeling in Mechanobiology 12 (3) 597–615.

[23] T.-Y. Kim, E. Puntel, E. Fried, Numerical study of the wrinkling of a stretched thin sheet, Int. J. Solids Struct. 49 (2012) 771–782.

[24] S. Fernández-Méndez, A. Huerta, Imposing essential boundary conditions in mesh-free methods, Comput. Methods Appl. Mech. Engrg. 193 (2004) 1257–1275.

[25] A. Hansbo, P. Hansbo, An unfitted finite element method, based on Nitsche's method, for elliptic interface problems, Comput. Methods Appl. Mech. Engrg. 191 (2002) 5537–5552.

[26] J. Dolbow, I. Harari, An efficient finite element method for embedded interface problems, Internat. J. Numer. Methods Engrg. 78 (2) (2009) 229–252.

[27] T.-Y. Kim, J.E. Dolbow, E. Fried, A numerical method of a second-gradient theory of incompressible fluid flow, J. Comput. Phys. 223 (2007) 551–570.

[28] T.-Y. Kim, J.E. Dolbow, An edge-bubble stabilized finite element method for fourth-order parabolic problems, Finite Elem. Anal. Des. 45 (2009) 485–494.

[29] T.-Y. Kim, J.E. Dolbow, E. Fried, Numerical study of the grain-size dependent Young's modulus and Poisson's ratio of bulk nanocrystalline materials, International Journal of Solids and Structures 49 (2012) 3942–3952.

[30] S.C. Brenner, L.R. Scott, The Mathematical Theory of Finite Element Methods, third ed., Springer-Verlag, New York, 2008.

[31] D.-W. Shin, Y. Jeon, E.-J. Park, A hybrid discontinuous Galerkin method for advection-diffusion-reaction problems, Appl. Numer. Math. 95 (2015) 292–303.

[32] M.D. Gunzburger, Finite Element Methods for Viscous Incompressible Flows: A Guide to Theory, Practice, and Algorithms, Academic Press, 1989.

[33] F. Fairag, A two-level finite-element discretization of the stream function form of the Navier–Stokes equations, Comput. Math. Appl. 36 (1998) 117–127.

[34] F. Fairag, N. Almulla, Finite element technique for solving the stream function form of a linearized Navier–Stokes equations using Argyris element, 2004. arXiv:math/0406070.

[35] P.F. Cummins, Inertial gyres in decaying and forced geostrophic turbulence, J. Mar. Res. 50 (1992) 545–566.

[36] T. Warburton, J.S. Hesthaven, On the constants in hp-finite element trace inverse inequalities, Comput. Methods Appl. Mech. Engrg. 192 (25) (2003) 2765–2773.

[37] P.G. Myers, A.J. Weaver, A diagnostic barotropic finite-element ocean circulation model, J. Atmos. Ocean. Technol. 12 (1995) 511–526.

[38] J.M. Cascón, G.C. Garcia, R. Rodriguez, A priori and a posteriori error analysis for a large-scale ocean circulation finite element model, Comput. Methods Appl. Mech. Engrg. 192 (2003) 5305–5327.